# Coexistence of ferroelectricity and antiferroelectricity in lead zirconate titanate

T. Asada and Y. Koyama
*Kagami Memorial Laboratory for Materials Science and Technology, and Department of Materials Science and Engineering, Waseda University, Tokyo, 169-0051, Japan*

(Received 10 March 2004; revised manuscript received 30 April 2004; published 15 September 2004)

The stability balance among the ferroelectric, ferrielectric, and antiferroelectric phases in dielectric materials has been studied by concretely examining the crystallographic features of $Pb(Zr_{1-x}Ti_x)O_3$ samples with $0.07 \leqslant x \leqslant 0.20$ by transmission electron microscopy. It was, as a result, found that in this oxide system the increase in the degree of antiferroelectricity into the ferroelectric state resulted in the unique sequence of the phase changes including the appearance of the two-phase state and two ferrielectric phases.

DOI: 10.1103/PhysRevB.70.104105 PACS number(s): 64.70.Kb, 77.90.+k, 68.37.Lp

In the antiferroelectric state, lines of ions in the crystal are spontaneously polarized, but with neighboring lines polarized in antiparallel directions.[1] The discussion of the thermodynamic stability of antiferroelectricity started with Kittel and Cross in the 1950's.[1,2] Based on the Landau theory for the pseudocubic perovskite oxides, particularly, Cross obtained ten solutions including the ferrielectric states, in addition to the ferroelectric and antiferroelectric states. Even nowadays, the stability balance among the ferroelectric, ferrielectric, and antiferroelectric states is still one of the fascinating subjects in dielectric materials.[3–10]

Among simple perovskite oxides, it was reported that the ferroelectric and antiferroelectric phases are present in $Pb(Zr_{1-x}Ti_x)O_3$ (PZT).[11,12] Recently we found the ferroelectric incommensurate phase in $0 \leqslant x \leqslant 0.10$.[13,14] The analysis of its crystallographic features revealed that the incommensurate phase interestingly has the ferrielectric character, which is characterized by both the $\Gamma_{15}$ ferroelectric displacement along the $[001]_c$ direction and the $M_5'$ antiferroelectric displacement in the $(001)_c$ plane. Note that the subscript $c$ denotes the pseudocubic system. This character exactly corresponds to one of the Cross's ferrielectric solutions mentioned above. In addition, the normal phase of the incommensurate phase should also have the ferrielectric character because the incommensurate phase just appears by introducing only the $M_3$ rotational displacement of the oxygen octahedra into the normal phase. In order to understand the stability balance among these normal and incommensurate phases as well as the ferroelectric and antiferroelectric phases, we have examined the crystallographic features of PZT samples with $0.07 \leqslant x \leqslant 0.20$ by transmission electron microscopy. It should be noted that because of the abovementioned characters the normal and incommensurate phases are, respectively, referred to as the ferrielectric normal (FN) and ferrielectric incommensurate (FI) phases in this paper.

In this study, PZT samples with $0 \leqslant x \leqslant 0.20$ were prepared by a conventional solid-state reaction. A mixture of PbO, $ZrO_2$, and $TiO_2$ powders was pressed into pellets and calcinated at 1173 K for 1 h. The sintering was made at 1448 K for 16 h. Dielectric measurements for the prepared samples were carried out, using a HIOKI LCR meter. Ar-ion milled samples coated with carbon films were provided for transmission-electron-microscopy studies. Observation was actually made, by using a JEM-3010 transmission electron microscope equipped with a high-temperature holder and imaging plates as a recording medium. It should be noted here that the transmission electron microscope is not an experimental method, which is familiar with the field of dielectric materials. The advantage of the use of the microscope is, however, to elucidate both spatial distributions of ferroelectric- and antiferroelectric-displacement regions and a direction of a polarization vector in each ferroelectric region by means of the dark field technique. This advantage actually made it possible to find new ferroelectric and ferrielectric states in PZT. Before describing the experimental data obtained in this study, below we simply explain the reason why the direction of the polarization vector can be determined by transmission electron microscopy.

The determination of the polarization-vector direction can be made with the help of the failure of the Friedel's law. When intensities of two reflections with reciprocal lattice vectors of $\mathbf{g}$ and $-\mathbf{g}$ are, respectively, written as $I_{\mathbf{g}}$ and $I_{-\mathbf{g}}$, the Friedel's law expressed as $I_{\mathbf{g}}=I_{-\mathbf{g}}$ is valid even in crystals having no center of symmetry in the kinematical theory of diffraction. However, Fujimoto pointed out that the law is failed in the dynamical effect.[15] In ferroelectric crystals, dark field images taken by reflections with $\mathbf{g}\cdot\mathbf{P}s>0$ under the two-beam condition concretely give rise to bright contrast for the ferroelectric region with the polarization $\mathbf{P}s$.[16] We thus determined the direction of $\mathbf{P}s$ in each ferroelectric-displacement region by taking dark field images under this imaging condition in this study.

Figure 1(a) shows the Zr-rich portion of the phase diagram of PZT, which was determined on the basis of our experimental data. According to the diagram, there are both the FI and FN phases each existing as a ferrielectric phase between the pure antiferroelectric (AF) and high-temperature rhombohedral ferroelectric (HTRF) phases just below the Curie temperature $T_c$. The two-phase (TP) state exists between the HTRF and FN phases. Note that the low-temperature rhombohedral ferroelectric (LTRF) phase is also present below the stable regions of the HTRF, FN, and FI phases in $x>0.05$ of this phase diagram. The characteristic feature is that, as was mentioned above, the FI phase is produced by the introduction of the $M_3$ rotational displacement

 

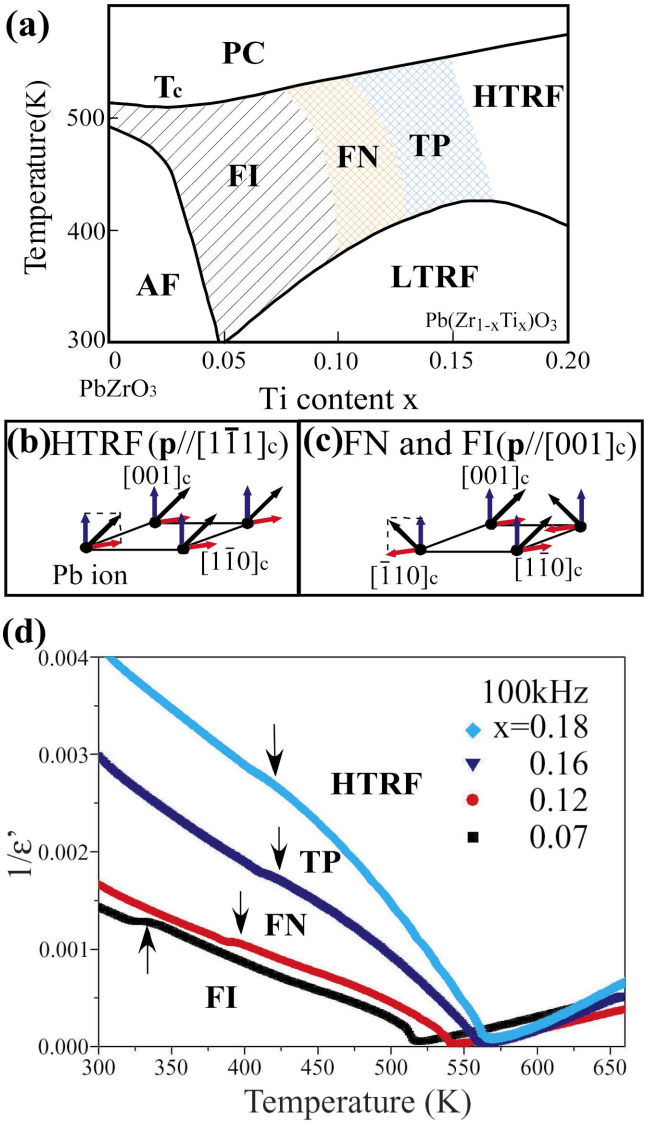


FIG. 1. (Color) Phase diagram and the dielectric properties of $Pb(Zr_{1-x}Ti_x)O_3$. (a) the Zr-rich portion of the phase diagram in $0 \leqslant x \leqslant 0.20$. (b) and (c), the atomic displacements of the Pb ions in the HTRF phase with the $[111]_c$ polarization and the FN and FI phases with the $[001]_c$ polarization. The blue and red arrows represent the components of the displacements along the $[001]_c$ direction and in the $(001)_c$ plane, respectively. The resultant displacement of each Pb ion is indicated by the black arrow. (d), the inverse curves of a real dielectric permittivity with 100 kHz as a function of temperature for $x=0.18$, 0.16, 0.12, and 0.07.

into the FN phase involving both the $\Gamma_{15}$ ferroelectric and $M_5'$ antiferroelectric displacements.[13,14] The polarization vectors in the FN and FI phases are parallel to one of the $\langle 001 \rangle_c$ directions, while the HTRF phase as a pure ferroelectric phase has the $\langle 111 \rangle_c$ polarization. The atomic displacements of the Pb ions in the HTRF phase with the $[11\bar{1}]_c$ polarization and the FN phase (the FI phase) with the $[001]_c$ polarization are depicted in Figs. 1(b) and 1(c), respectively. As can be seen in the diagrams, the ferroelectric-displacement component in the $(001)_c$ plane of the HTRF phase is converted to the antiferroelectric-displacement component in the FN and FI phases. The appearance of the TP state should thus be associated with the ferroelectric- to antiferroelectric-displacement conversion.

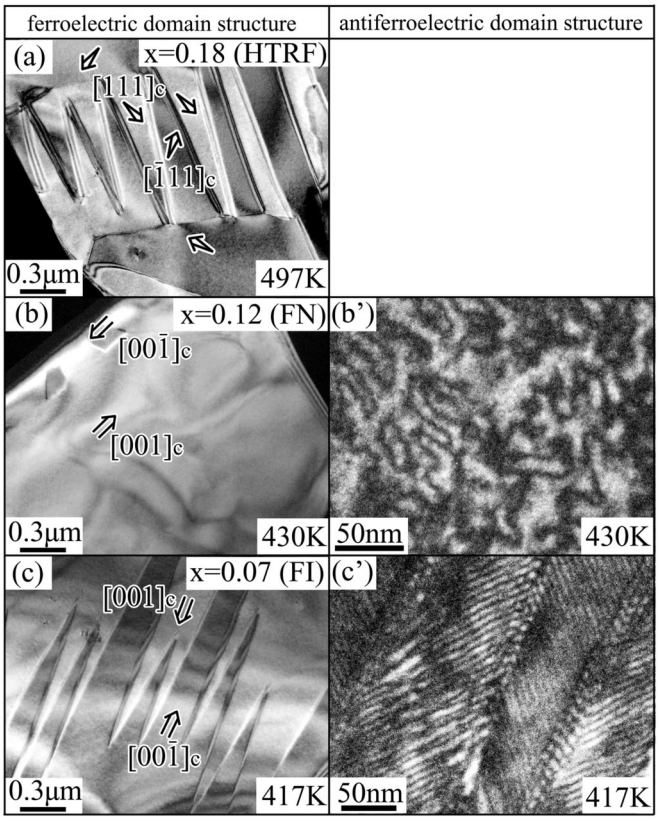


FIG. 2. Dark field images showing the ferroelectric and antiferroelectric domain structures in the $x=0.18$, 0.12, and 0.07 samples, which have the HTRF, FN, and FI phases, respectively.

The inverse curves for the real dielectric permittivity $\varepsilon'$ with 100 kHz in the $x=0.18$ (HTRF), 0.16 (TP), 0.12 (FN), and 0.07 (FI) samples, obtained in the cooling process from the paraelectric cubic (PC) phase, are shown in Fig. 1(d). The transition temperature to the LTRF phase in each sample is marked by the arrow. As seen in the figure, the inverse curves for these samples exhibit the systematic change below $T_c$. For instance, the value of the slope of each curve below $T_c$ decreases with decreasing Ti content. The $x=0.16$ sample with the TP state has an intermediate slope between the $x=0.18$ and 0.12 samples. The highest transition temperature to the LTRF phase seems to be obtained in $x=0.16$ near the HTRF/TP boundary.

The ferroelectric and antiferroelectric domain structures of the HTRF ($x=0.18$), FN ($x=0.12$), and FI ($x=0.07$) phases are shown in Fig. 2. Figure 2(a) is the dark field image for the ferroelectric domain structure in the HTRF phase with the $\langle 111 \rangle_c$ polarization vectors. The image was taken from the $x=0.18$ sample at 497 K by using the $110_c$ fundamental reflection with the $[001]_c$ electron incidence. It is obvious that an antiferroelectric domain is absent in the HTRF phase because of the pure ferroelectric phase. In the image, banded-contrast regions due to ferroelectric domains

are seen, together with fringes in the boundaries between two neighboring banded regions. These features were confirmed to be entirely consistent with the ferroelectric domain structure with the $\langle 111\rangle_c$ polarization vectors. The determined direction of the vector in each domain is depicted by the arrow. When the Ti content $x$ is lowered from $x=0.18$, then the FN phase as a ferrielectric phase appears around $x=0.12$ via the TP state. The ferroelectric and antiferroelectric domain structures in the FN phase are shown in the dark field images of the $x=0.12$ sample at 430 K. The ferroelectric- and antiferroelectric- domain-structure images in Fig. 2(b) and 2(b′) were, respectively, taken by the $002_c$ reflection with the $[010]_c$ incidence and the $3/2\ 1/2\ 0_c$ superlattice reflection with the $[133]_c$ incidence. Note that the superlattice reflection is due to the $M_5'$ antiferroelectric displacement. The feature of the ferroelectric domain structure in Fig. 2(b) is that large ferroelectric domains with $\langle 001\rangle_c$ polarization vectors are observed, corresponding to the $\langle 001\rangle_c$ polarization in the FN phase. No domain with the $\langle 111\rangle_c$ polarization is detected in the $x=0.12$ sample at all. As for the antiferroelectric domains structure in Fig. 2(b′), we see a random array of dark-contrast lines identified as an antiphase boundary for the $M_5'$ antiferroelectric displacement in the $\{001\}_c$ planes. In the $x=0.07$ sample of the FI phase, further, there are ferroelectric and antiferroelectric domain structures in the dark field images, Figs. 2(c) and 2(c′), respectively. The conditions for taking these images are the same as those in the $x=0.12$ sample. The ferroelectric domains in the FI phase, Fig. 2(c), have the $\langle 001\rangle_c$ polarization, just as in the case of the FN phase. On the other hand, the characteristic feature of the antiferroelectric domain structure in the FI phase is that the antiphase boundaries are arranged periodically. As was described in our previous paper,[13,14] the periodic array of the antiphase boundaries characterizing the incommensurate modulation originates from the alternating array of two microdomains for the $M_3$ rotational displacement of the oxygen octahedra.

In the present study, the TP state was found to exist in $0.12\leqslant x\leqslant 0.16$ between the HTRF and FN phases. In order to understand the detailed features of the TP state, the spatial distribution of the antiferroelectric-displacement component was first examined by taking dark field images using the $3/2\ 1/2\ 0_c$ superlattice reflections in the $[133]_c$ electron incidence. Figure 3 shows a series of the obtained images as functions of temperature and Ti content $x$. Local bright regions involving the antiferroelectric displacement are seen in these images. The features of the local regions are that their average size is estimated to be 5–10 nm, and that both the lowering of temperature and the decrease in the Ti content result in the increase in the number of the local regions. In other words, the local regions characterizing the antiferroelectric displacement are mainly developed by their coalescence; that is, the percolative-type mechanism.

The detailed features of the ferroelectric-displacement component in the TP state were examined with the help of the failure of the Friedel's law.[15] It was found that, in samples composed of crystal grains with sizes more than 2 $\mu$m, there are two types of grains with the polarization

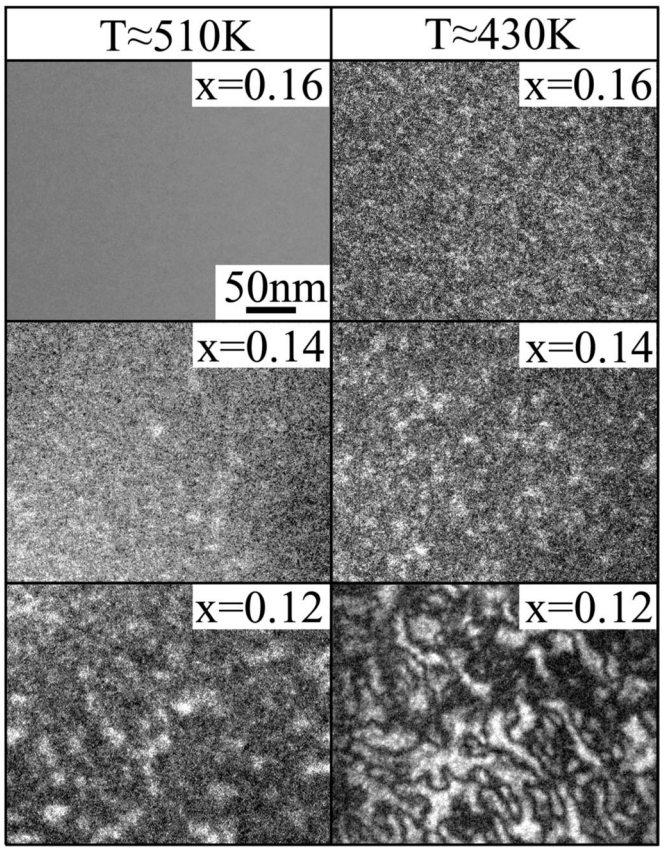


FIG. 3. Development of the antiferroelectric-displacement regions in the TP state with $0.16\geqslant x\geqslant 0.12$. The antiferroelectric domain structure of the FN phase in the $x=0.12$ sample at 430 K, Fig. 2(b′), is understand to result from the increase in the number of the local antiferroelectric-displacement regions.

vectors parallel to the $\langle 102\rangle_c$ and $\langle 001\rangle_c$ directions, instead of the $\langle 111\rangle_c$ polarization in the HTRF phase. The point to be noted here is that, in the $x=0.16$ sample the number of the $\langle 102\rangle_c$ grains is much larger than that of the $\langle 001\rangle_c$ grains, while the $\langle 001\rangle_c$ grains are dominant in the other samples of the TP state. No grain consisted of two regions with the $\langle 102\rangle_c$ and $\langle 001\rangle_c$ polarizations at all. These facts indicate that each crystal grain in the samples has a slightly different Ti content. In addition, because the number of $\langle 102\rangle_c$ grains rapidly decreases with decreasing Ti content, the $\langle 102\rangle_c$ polarization should be stabilized only around $x=0.16$; that is, near the HTRF/TP boundary. In the TP state with $0.12\leqslant x<0.16$, on the other hand, the ferroelectric displacement is parallel to one of the $\langle 001\rangle_c$ directions, just as in the case of the FN and FI phases. The $\langle 102\rangle_c$ domain structure in $x=0.16$ at 440 K and the $\langle 001\rangle_c$ structure in $x=0.14$ at 440 K are, respectively, shown in Figs. 4(a), 4(b′), and 4(c′). Under the two-beam condition, actually, the images with the $[211]_c$ incidence in Figs. 4(a) and 4(a′) were, respectively, taken by the $102_c$ and $\bar{1}0\bar{2}_c$ reflections, and those with the $[010]_c$ incidence in 4(b) and 4(b′) by the $002_c$ and reflections. As seen in the figure, the notable feature of the $\langle 102\rangle_c$ ferroelectric

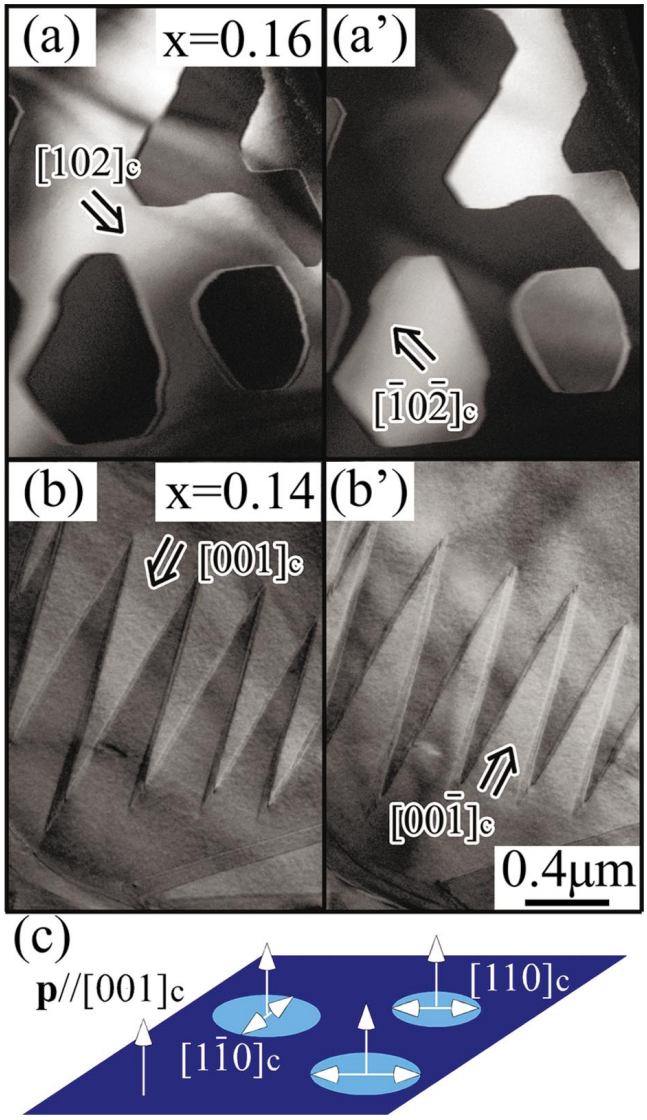


FIG. 4. (Color) Two ferroelectric states appearing in the TP state, together with the schematic diagram showing the TP state. The ferroelectric domain structure in the $x=0.16$ sample at 440 K, Figs. 4(a) and 4(a′), has the $\langle 102\rangle_c$ polarization, while the $\langle 001\rangle_c$ polarization is obtained in the domain structure in the $x=0.14$ sample at 440 K, (b) and (b′). In (c), the directions of the polarization vector and the atomic shifts for the $M_5{}'$ antiferroelectric displacement are, respectively, denoted by the single and double arrows. The TP state in $0.16>x\geqslant 0.12$ consists of the local FN phase and the $[001]_c$ ferroelectric state.

domain structure is the presence of the round-shaped domains, and the $\langle 001\rangle_c$ domain structure is basically the same as in the FN and FI phases. The large number of dot contrasts with the average size of about 10 nm are also detected in the whole area of the $\langle 001\rangle_c$ domain structure in Figs. 4(b) and 4(b′), reflecting the presence of local antiferroelectric-displacement regions in the TP state. Because having the $\langle 001\rangle_c$ polarization, the local antiferroelectric-displacement region can be identified as the local FN phase, as shown in Fig. 4(c). It is thus understood that in the case of PZT the introduction of antiferroelectricity into the ferroelectric state first leads to the instability of the polarization component in the (001) plane, together with the appearance of the TP state. In the TP state, this instability results in the $\langle 102\rangle_c$ ferroelectric domain structure as the first step near the HTRF/TP boundary, and then the $\langle 001\rangle_c$ domain structure as the second step, with the increase in the number of the local FN-phase regions as a ferrielectric phase.

Our experimental findings provide the instability of a certain component of the polarization when antiferroelectricity is introduced into the ferroelectric state. In the case of PZT, as a result of the instability of the (001)-plane polarization component, both the TP state, and the FN and FI phases as a ferrielectric phase appear just below $T_c$ between the HTRF and AF phases. The notable features of the TP state consisting of the ferrielectric and ferroelectric states are that the ferrielectric state is the local FN phase, and that there are two ferroelectric states. One is the ferroelectric state with the $\langle 102\rangle_c$ polarization only around $x=0.16$ near the HTRF/TP boundary, where the degree of antiferroelectricity must be very weak. The finding of the $\langle 102\rangle_c$ ferroelectric state is the first in ferroelectric materials. The other state has the $\langle 001\rangle_c$ polarization in $0.12\leqslant x<0.16$, just as in the FN and FI phases. The $\langle 001\rangle_c$ state should be characterized by large fluctuation of the polarization in the $(001)_c$ plane. In the TP state with this large fluctuation, then the antiferroelectric-displacement component in the $(001)_c$ plane of the FN phase is mainly developed by the percolative-type mechanism with the increasing degree of antiferroelectricity. Based on these experimental results, the increase in antiferroelectricity in PZT leads to the fascinating sequence of the phase changes from the pure ferroelectric phase to the pure antiferroelectric phase via the TP state and two ferrielectric phases.

Finally, we simply discuss the origin of the appearance of the $[102]_c$ ferroelectric state, which was found in the TP state near the HTRF/TP boundary. As was mentioned above, the appearance of the state should be associated with the instability of the $(001)_c$ component of the $[111]_c$ polarization in the HTRF phase; that is, the change in the direction of the polarization vector $[111]_c\rightarrow[001]_c$. This instability is thus equivalent to the situation that the electric field along the $[001]_c$ direction is applied to the ferroelectric state with the $[111]_c$ polarization. It should be remarked that this situation is in contrast with that near the morphotropic phase boundary (MPB) around $x=0.50$. The latter near the MPB corresponds to the application of the field of the $[111]_c$ orientation to the state with the $[001]_c$ polarization. According to the first-principle calculation made by Bellaiche *et al.*,[17] the change in the direction of the polarization vector in the former application involves the appearance of the *A*-type monoclinic, triclinic, and the *C*-type monoclinic states, while only the *A*-type monoclinic state is expected as an intermediates state in the latter. Because belonging to the *C*-type monoclinic group, the $[102]_c$ ferroelectric state is understood to be entirely consistent with the theoretical suggestion made by them.

[1] C. Kittel, Phys. Rev. **82**, 729 (1951).
[2] L. E. Cross, Philos. Mag. **1**, 76 (1956).
[3] Yu. M. Vysochanskii, V. A. Stephanovich, A. A. Molnar, V. B. Cajipe, and X. Bourdon, Phys. Rev. B **58**, 9119 (1998).
[4] R. Ranjan, D. Pandey, and N. P. Lalla, Phys. Rev. Lett. **84**, 3726 (2000).
[5] E. Collet, M. Buron-LeCointe, M. H. Lemée-Cailleau, H. Cailleau, L. Toupet, M. Meven, S. Mattauch, G. Heger, and N. Karl, Phys. Rev. B **63**, 054105 (2001).
[6] L.-H. Ong, J. Osman, and D. R. Tilley, Phys. Rev. B **65**, 134108 (2002).
[7] S. Miao, J. Zhu, X. Zhang, and Z.-Y. Cheng, Phys. Rev. B **65**, 052101 (2002).
[8] V. M. Ishchuk, Ferroelectrics **289**, 1 (2003).
[9] V. M. Ishchuk, Ferroelectrics **289**, 33 (2003).
[10] H. M. Christen, E. D. Specht, S. S. Silliman, and K. S. Harshavardhan, Phys. Rev. B **68**, 020101 (2003).
[11] D. Viehland, Phys. Rev. B **52**, 778 (1995).
[12] X. Dai, Z. Xu, and D. Viehland, J. Am. Ceram. Soc. **78**, 2815 (1995).
[13] S. Watanabe and Y. Koyama, Phys. Rev. B **63**, 134103 (2001).
[14] S. Watanabe and Y. Koyama, Phys. Rev. B **66**, 134102 (2002).
[15] F. Fujimoto, J. Phys. Soc. Jpn. **14**, 1558 (1959).
[16] M. Tanaka and G. Honjo, J. Phys. Soc. Jpn. **19**, 951 (1964).
[17] L. Bellaiche, Alberto García, and David Vanderbilt, Phys. Rev. B **64**, 060103(R) (2001).